

On microstructure-property relationships derived by virtual materials testing with an emphasis on effective conductivity

Matthias Neumann^{1*}, Orkun Furat¹, Dzmitry Hlushkou^{2**}, Ulrich Tallarek^{2**}, Lorenz Holzer³, and Volker Schmidt^{1*}

¹ Institute of Stochastics, Ulm University, Helmholtzstraße 18, D-89069 Ulm, Germany

² Department of Chemistry, Philipps-Universität Marburg, Hans-Meerwein-Straße 4, D-35032 Marburg, Germany

³ Institute of Computational Physics, ZHAW, Wildbachstrasse 21, CH-8400 Winterthur, Switzerland

Abstract. Based on virtual materials testing, which combines image analysis, stochastic microstructure modeling and numerical simulations, quantitative relationships between microstructure characteristics and effective conductivity can be derived. The idea of virtual materials testing is to generate a large variety of stochastically simulated microstructures in short time. These virtual, but realistic microstructures are used as input for numerical transport simulations. Finally, a large data basis is available to study microstructure-property relationships quantitatively by classical regression analysis and tools from statistical learning. The microstructure-property relationships obtained for effective conductivity can also be applied to Fickian diffusion. For validation, we discuss an example of Fickian diffusion in porous silica monoliths on the basis of 3D image data.

1 Introduction

The functionality of many materials, like, e.g., solar cells [1], batteries [2], fuel cells [3] or silica monoliths used for catalysis [4], is strongly influenced by their microstructure. Thus an optimal design of the microstructure regarding effective macroscopic properties of these materials would lead to an improvement of their functionality. This kind of microstructure optimization, in turn, requires an understanding of the quantitative relationships between microstructure characteristics and effective macroscopic properties, which are – so far – only available for some special types of simple microstructures [5] like, e.g., the coated spheres model introduced in [6].

* The work of MN and VS has been partially funded by the German Federal Ministry for Economic Affairs and Energy (BMWi) under grant 03ET6095E.

** The work of DH and UT has been supported by the Deutsche Forschungsgemeinschaft DFG (Bonn, Germany) under grant TA 268/9-1.

A direct approach to investigate relationships between microstructure and effective macroscopic properties is based on tomographic 3D imaging of microstructures. Among other methods, X-ray tomography [7], FIB-SEM tomography [8] and STEM tomography [9] provide highly resolved information about microstructures on different length scales. On the one hand, 3D image data can be analyzed by tools from spatial statistics [10] and mathematical morphology [11], which allows the computation of well-defined microstructure characteristics. On the other hand, 3D image data can be used as an input information for the numerical simulation of effective macroscopic properties, like, e.g., effective diffusivity in silica monoliths [12]. This combination of image analysis and numerical simulation enables a direct investigation of the relationship between well-defined microstructure characteristics and effective macroscopic properties [12–16]. However, this approach is limited as it is not possible to investigate a sufficiently large data set of different microstructures due to the high costs of 3D imaging.

Thus an alternative approach – called virtual materials testing – was suggested where image analysis and numerical simulations are combined with stochastic 3D microstructure modeling [17]. By the aid of stochastic modeling virtual, but realistic, microstructures can be generated in short time. So a large data set of virtual microstructures with a wide range of microstructure characteristics is generated in order to study the quantitative relationship between microstructure characteristics and effective macroscopic properties efficiently. In the present paper, we give an overview of the results having been obtained for the microstructure influence on electric conductivity by virtual materials testing [17–19]. Furthermore, we show how the results can be used to predict effective diffusivity in silica monoliths.

Before we give a detailed description on how to simulate the considered stochastic 3D microstructure model in Sect. 3, the microstructure characteristics which are related to effective conductivity are described in Sect. 2. The results of virtual materials testing with respect to electric conductivity are reviewed in Sect. 4. It is shown in Sect. 5 that the results can be used to predict effective diffusivity in silica monoliths the morphology of which has been analyzed in [20]. Conclusions are given in Sect. 6.

2 Microstructure Characteristics and M -factor

To investigate the microstructure influence on effective conductivity σ_{eff} we consider the microstructure characteristics volume fraction ε , mean geometric tortuosity τ_{geom} , mean geodesic tortuosity τ_{geod} and constrictivity β . These microstructure characteristics are computed based on voxelized 3D images representing (virtual or real) microstructures. Moreover, using $\varepsilon, \tau_{\text{geom}}, \tau_{\text{geod}}, \beta$ the M -factor

$$M = \sigma_{\text{eff}}/\sigma_0 \quad (1)$$

is predicted, where σ_0 denotes the intrinsic conductivity of the considered material.

2.1 M -factor

As described in [18], we consider conductive transport processes within porous materials with one conducting phase, the intrinsic conductivity of which is σ_0 .

Let J denote the current density, σ the space-dependent conductivity function, U the electric potential and t the time. Then, electric charge transport is described by Ohm's law

$$J = -\sigma \frac{\partial U}{\partial x} \quad (2)$$

and

$$\frac{\partial U}{\partial t} = \sigma \frac{\partial^2 U}{\partial x^2}. \quad (3)$$

Assuming constant boundary conditions, such systems converge to an equilibrium which is described by the Laplace equation

$$\Delta U = 0. \quad (4)$$

By averaging over J and U as described in [5] we obtain the effective conductivity σ_{eff} and thus the M -factor of the microstructure. For the numerical simulation of M the software NM-SESES [21] has been used in [17], while GeoDict [22] has been used in [18, 19].

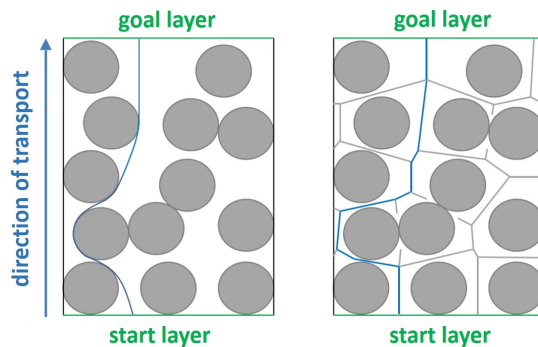


Fig. 1. Visualization of two different kinds of shortest path corresponding to τ_{geom} (center, right) and τ_{geod} (left) in 2D. The conducting phase is represented in white, while sphericle obstacles are represented in grey. The shortest paths from the start layer to the goal layer are visualized in blue. The skeleton on which the paths for τ_{geom} are computed is represented by a grey network (right).¹

¹ Reprinted from [18], Figure 3, with permission of J. Wiley & Sons.

2.2 Tortuosity

Both characteristics, τ_{geom} and τ_{geod} describe the length of paths through the conducting phase relative to the thickness of the material. Note that – in contrast to concepts of effective tortuosity – the characteristics τ_{geom} and τ_{geod} depend only on the geometry of the microstructure. An overview on the available concepts of tortuosity in the literature is given in [23]. To determine τ_{geod} , we compute for each voxel of the conducting phase located at the start layer, i.e. the plane where the conduction process starts, the shortest path through the conducting phase to the goal layer in terms of geodesic distance [24]. Such a shortest path is visualized in Fig. 1(left). Mean geodesic tortuosity τ_{geod} is defined as the average of these path lengths divided by the thickness of the material. Mean geometric tortuosity τ_{geom} is also defined as an average of shortest path lengths, where shortest paths are computed on a skeleton of the conducting phase, see Fig. 1(right). The skeleton of a microstructure is a network of medial axes through the conducting phase [24]. In [17] and [18] the software Avizo [25] has been used to extract the skeleton from 3D image data.

2.3 Constrictivity

Constrictivity β quantifies bottleneck effects. It has been defined for a single tube with periodic constrictions in [26] by $\beta = (r_{\text{min}}/r_{\text{max}})^2$, where r_{min} and r_{max} are the radius of the minimum and maximum cross-section of the tube, respectively. This concept of constrictivity has been generalized defining $r_{\text{min}}, r_{\text{max}}$ and thus β for complex microstructures [27]. As described in [19], r_{max} is defined as the 50% quantile of the continuous pore size distribution, while r_{min} is defined as the 50% quantile of the MIP pore size distribution, which is based on a geometrical simulation of mercury intrusion porosimetry, introduced in [28]. Constrictivity takes values between 0 and 1, where values close to 0 indicate strong bottleneck effects while values close to 1 indicate that there are no bottlenecks at all.

3 Stochastic 3D Microstructure Model

In [17], a parametric stochastic 3D microstructure model has been developed, which has been used to simulate virtual microstructures with many different constellations for the microstructure characteristics $\varepsilon, \tau_{\text{geom}}$ (or τ_{geod}) and β . We recall the definition of the model introduced in [17] and give a detailed description on how to simulate model realizations.

3.1 Model Definition

Using tools of stochastic geometry and graph theory, we define a random set Ξ representing the conducting phase of a microstructure. At first a random geometric graph $G = (V, E)$ is modeled consisting of a set of vertices V and a set of edges E , which are connections between the vertices. In a second step the

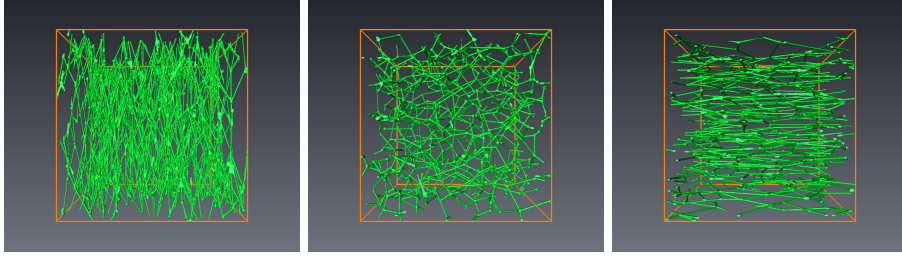


Fig. 2. Generalized RNG, where the set of vertices is given by a realization of a homogeneous Poisson point process. The parameter α is chosen as $\alpha = -5$ (left, vertically oriented edges), $\alpha = 0$ (center, no preferred orientation of edges), and $\alpha = 5$ (right, horizontally oriented edges). Direction $(0, 0, 1)$ is the direction from front to back.²

edges of the graph are randomly dilated to get a full-dimensional conducting phase.

The set of vertices V is modeled by a homogeneous Poisson point process with some intensity $\lambda > 0$, see e.g. [29]. This means that the vertices are distributed completely at random in the three-dimensional space and the expected number of points per unit volume is given by λ . Edges between pairs of vertices are put according to the rule of a generalized relative neighborhood graph (RNG) introduced in [17]. For a parameter $\alpha \in \mathbb{R}$, two vertices $v_1, v_2 \in V$ are connected by an edge if there is no other vertex $v_3 \in V \setminus \{v_1, v_2\}$ such that

$$d_\alpha(v_1, v_2) > \max\{d_\alpha(v_1, v_3), d_\alpha(v_2, v_3)\}, \quad (5)$$

where

$$d_\alpha(v_1, v_2) = d(v_1, v_2) \max \left\{ 0.01, \left(1 - \frac{2\varphi(v_1, v_2)}{\pi} \right)^\alpha \right\}, \quad (6)$$

$d(v_1, v_2)$ denotes the Euclidean distance from v_1 to v_2 , and $\varphi(v_1, v_2)$ denotes the acute angle between the line segments $v_2 - v_1$ and $(0, 0, 1)$. By the aid of the model parameter α , it is possible to control the directional distribution of edges in the graph G and thus one can control τ_{geom} and τ_{geod} in the virtual microstructure. Note that for $\alpha = 0$ we are in the situation of the classical RNG [30], i.e., there is no preferred orientation of the edges. For $\alpha > 0$ we obtain more edges oriented in direction $(0, 0, 1)$ than for $\alpha < 0$, see Fig. 2.

In order to result in a full-dimensional conducting phase each edge of G is dilated by a sphere with random radius. The dilation radii are independently and identically distributed (i.i.d) following a Gamma-distribution with mean value $g_1 > 0$ and variance $g_2 > 0$. The Gamma-distribution is shifted by 1 to ensure that each edge is at least dilated by a ball of radius 1. Formally, we result in a conducting phase

$$\Xi = \bigcup_{e \in E} e \oplus B(o, R_e), \quad (7)$$

² Reprinted from [17], Figure 5, with permission of J. Wiley & Sons.

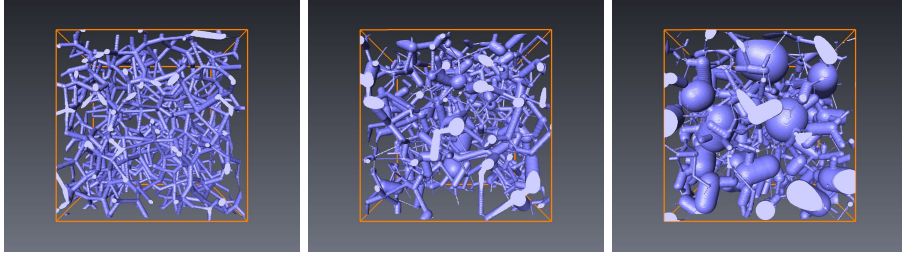


Fig. 3. Three realizations of the final conducting phase, where λ , α and g_1 are constant. Only the parameter g_2 is varied, that is $g_2 = 1$ (left), $g_2 = 4$ (center), and $g_2 = 7$ (right).³

where \oplus denotes the Minkowski addition of sets, R_e denotes the random dilation radius corresponding to the edge $e \in E$, and $B(o, r)$ denotes the (closed) ball centered at the origin $o \in \mathbb{R}^3$ with radius $r > 0$. While the volume fraction of Ξ can be controlled by the intensity $\lambda > 0$ and g_1 , constrictivity can be controlled by g_2 . The larger the variance of the dilation radii is, the more bottlenecks are created in the conductive phase, see Fig. 3.

3.2 Simulation of Model Realizations

Having defined the stochastic 3D microstructure model, the simulation of model realizations is described. In the following we assume algorithms for the simulation of uniformly distributed, Poisson distributed and Gamma distributed random variables to be known. For simulation of random variables the reader is referred to [31]. To simulate a realization of Ξ in a cuboid $W = [0, w]^3$ for given model parameters $\lambda, \alpha, g_1, g_2$, we simulate the generalized RNG G at first. The graph G is simulated based on a realization of vertices in a larger observation window $W^+ = [-\delta, w + \delta]^3$ for some $\delta > 0$ in order to avoid edge effects. Note that this approach approximates a realization of Ξ since in general, we can not guarantee that vertices located outside of W^+ do not influence the conductive phase in W , i.e., the random set $\Xi \cap W$. Nevertheless, the approximation error becomes neglectable in practice for sufficiently large W^+ .

To simulate G we begin with the simulation of the set of vertices $V = \{v_1, \dots, v_N\}$ in W^+ , where N is the random number of vertices in W^+ . That means that a homogeneous Poisson process has to be simulated in W^+ .

Algorithm 1 (Simulation of vertices [29]). *Let $\lambda > 0$ be the intensity of the homogeneous Poisson point process. Then, the set of vertices is simulated in W^+ by the following two step approach*

1. *Simulate a realization n of the random number N of vertices in W^+ , which is Poisson distributed with parameter $\lambda(w + 2\delta)^3$.*

³ Reprinted from [17], Figure 6, with permission of J. Wiley & Sons.

2. For each $i \in \{1, \dots, n\}$, simulate the position of the i -th vertex v_i , which is uniformly distributed in W^+ . That is, v_i is a three-dimensional vector each entry of which is uniformly distributed in the interval $[-\delta, w + \delta]$.

For a given set of vertices V , the edges are put and their random dilation radii are simulated to obtain the full-dimensional conductive phase.

Algorithm 2 (Simulation of the full-dimensional conductive phase).

Consider the set of vertices $V = \{v_1, \dots, v_n\}$ simulated by Algorithm 1.

1. Check for all $1 \leq i < j \leq n$ whether v_i and v_j are connected by an edge in G according to Inequality (5).
2. Simulate the dilation radii for the edges, i.e., simulate a collection of i.i.d. Gamma distributed random variables with mean g_1 and variance g_2 resulting in a realization $\{r_e : e \in E\}$ of the random radii $\{R_e : e \in E\}$.
3. The set

$$W \cap \bigcup_{e \in E} e \oplus B(o, r_e) \quad (8)$$

is an approximation of a realization of $\Xi \cap W$.

4 Prediction of Effective Conductivity

A number of 43 virtual microstructures is generated with different constellations for the microstructure characteristics $\varepsilon, \tau_{\text{geom}}/\tau_{\text{geod}}$ and β . These virtual microstructures are used as an input for numerical simulations of the M -factor. As a result the prediction formulas

$$\widehat{M} = \min \left\{ 1, \max \left\{ 0, 2.03 \frac{\varepsilon^{1.57} \beta^{0.72}}{\tau_{\text{geom}}^2} \right\} \right\}, \quad (9)$$

and

$$\widehat{M} = \frac{\varepsilon^{1.15} \beta^{0.37}}{\tau_{\text{geod}}^{4.39}}. \quad (10)$$

for the M -factor have been obtained by regression analysis in [17] and [18], respectively. The mean absolute percentage error (MAPE) is 16% when using Eq. (9) and 18% when using Eq. (10). A visualization of the goodness of fit is given in Fig. 4.

On the one hand, a prefactor of 2.03 is necessary in Eq. (9) to obtain an adequate prediction of M by ε, β and τ_{geom} . On the other hand $2.03 \varepsilon^{1.57} \beta^{0.72} \tau_{\text{geom}}^{-2}$ is in general not within the interval $[0, 1]$ and has thus to be artificially restricted to $[0, 1]$. Moreover, τ_{geom} depends on the specific choice of the skeletonization algorithm and skeletonization might be problematic for microstructures with a large volume fraction of the conductive phase. Even if the MAPE of Eq. (9) is smaller than the one of Eq. (10), the conclusion of [18] is to prefer τ_{geod} rather than τ_{geom} as microstructure characteristic describing the length of transport paths, in particular for the prediction of the M -factor.

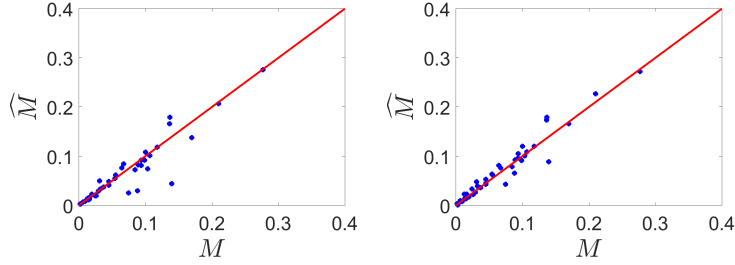


Fig. 4. Predicted M -factor \widehat{M} over numerically simulated M -factor M for the 43 virtual microstructures from [17,18]. Equation (9) (left) and Eq. (10) (right) are used to predict M .

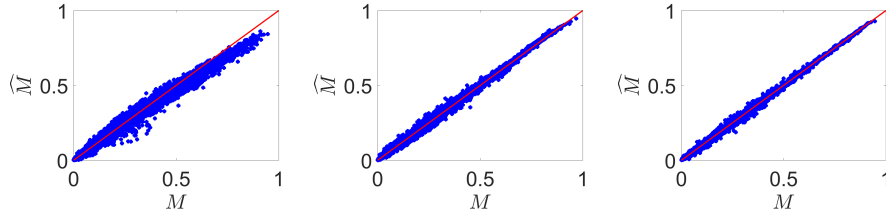


Fig. 5. Predicted M -factor \widehat{M} over numerically simulated M -factor M for the 8119 virtual microstructures from [19]. Classical regression analysis, i.e., Eq. (10) (left), as well as a trained neural network (center) and random forest (right) are used to predict M .⁴

An extension of this simulation study has been performed in [19], where 8119 virtual microstructures have been generated and the microstructure characteristics $\varepsilon, \beta, \tau_{\text{geod}}$ as well as the M -factor have been computed for each of them. Aside from the model presented in Sect. 3, the stochastic microstructure model from [32] has been used to generate virtual microstructures, where the conducting phase is a union of spherical particles or its complement. Considering different types of stochastic microstructure models, we want to ensure that the virtual testing approach is influenced by the specific kind of generating virtual microstructures as little as possible. It has been shown that the prediction of the M -factor can be further improved using methods from statistical learning [33], i.e. neural networks (9% MAPE) and random forests (8% MAPE), see Fig. 5. The MAPE of Eq. (10) reduces to 13% when all 8119 virtual structures are taken into account because then, the extreme microstructures play a less important role [17,18]. Furthermore, the extension of the simulation study has shown that Eq. (10) slightly underestimates the M -factors close to 1. Validation with experimental image data representing microstructures in SOFC anodes and microstructures in membranes of pH-sensors has been performed in [19], which

⁴ Reprinted from [19], Figure 6, with permission of J. Wiley & Sons.

shows that the prediction formulas are not only valid for model-based virtual microstructure.

5 Application to Fickian Diffusion in Silica Monoliths

For porous microstructures, there is a one-to-one relationship between effective conductivity and effective diffusivity of Fickian diffusion. We consider 3D image data of two different porous silica monoliths, in which Fickian diffusion takes place, as a further validation of the prediction formulas obtained by virtual materials testing. Since the diffusion takes place in the pores, the microstructure characteristics ε , τ_{geod} and β are computed for the pores in this section.

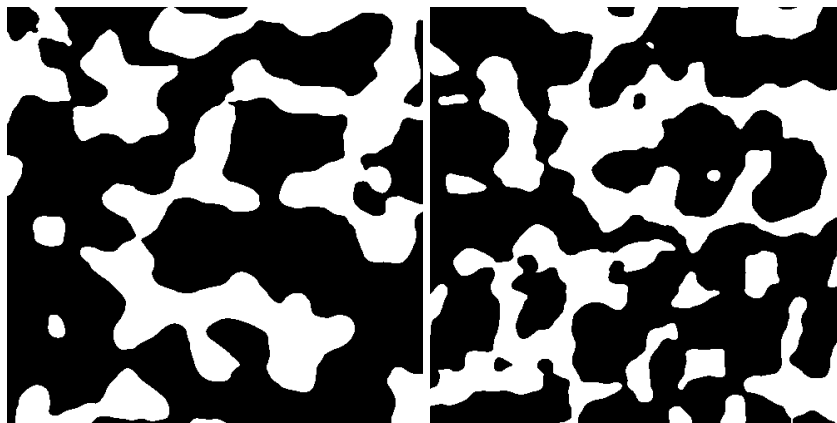


Fig. 6. Cutout of cross-sections ($15 \mu\text{m} \times 15 \mu\text{m}$) depicting the macropores (black) of the two silica monolith samples S_1 (left) and S_2 (right).

5.1 Description of the Material

The considered silica monoliths, manufactured by Merck, are used for high-performance liquid chromatography (HPLC) and catalysis. They consist of a single piece of silica with an interconnected pore phase, which contains macropores and mesopores [34]. Diffusion in the macropores is investigated based on tomographic image data of two samples, denoted by S_1 and S_2 with a resolution of 30 nm and sizes of $60 \times 60 \times 24.19 \mu\text{m}^3$ and $60 \times 60 \times 24.57 \mu\text{m}^3$, respectively. The mean size of the macropores is $1.36 \mu\text{m}$ in sample S_1 and $0.82 \mu\text{m}$ in sample S_2 . The image data depicting the macropores, see Fig. 6, is obtained via confocal laser scanning microscopy, see [12].

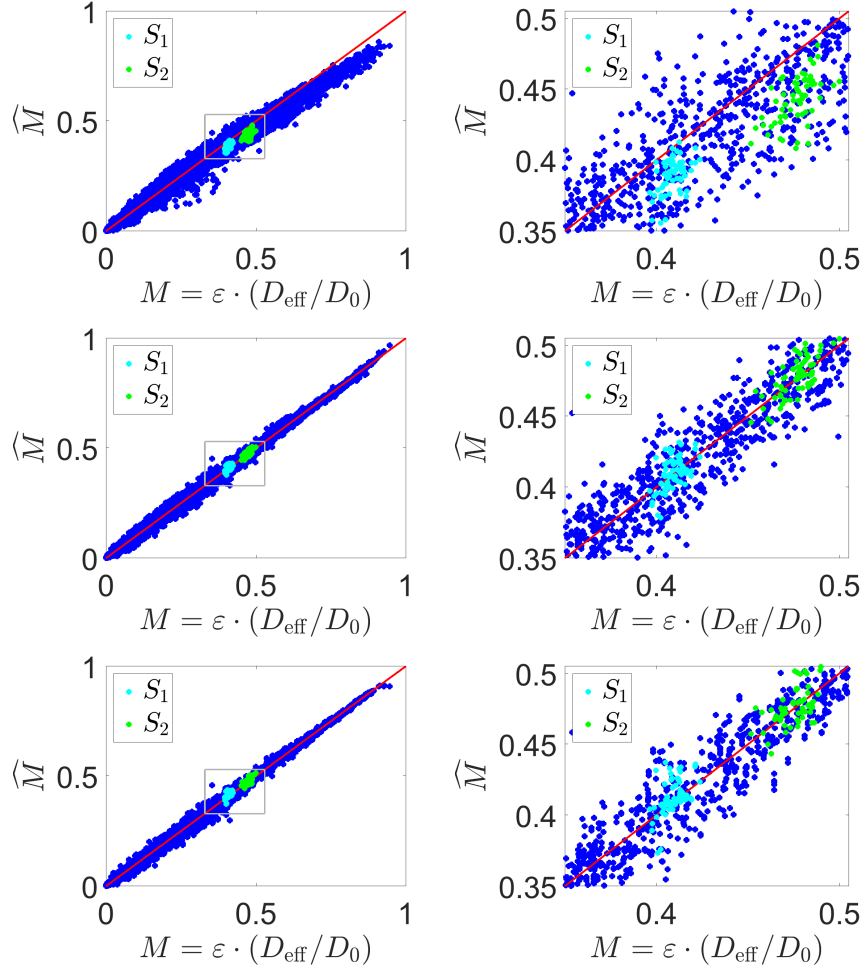


Fig. 7. The values of $M = \varepsilon D_{\text{eff}}/D_0$ computed by the random-walk particle-tracking algorithm are predicted using Eq. (10) (top), the neural network (center), and the random forest (bottom) from [19]. The values corresponding to the 8119 virtual microstructures (blue), to the cutouts from sample S_1 (cyan), and to the cutouts from sample S_2 (green) are represented in different colors. The right column shows a zoom to the square $[0.33, 0.53]^2$.

5.2 Effective Diffusivity

The diffusion process over time of a particle concentration u with intrinsic diffusivity D_0 in the pore phase can be analogously described to the conduction process, i.e. by the diffusion equation

$$\frac{\partial u}{\partial t} = D_{\text{eff}} \Delta u, \quad (11)$$

where D_{eff} denotes the effective diffusivity of the pore space. Due to the analogy between effective diffusivity and effective conductivity, the following relationship

$$M = \varepsilon \frac{D_{\text{eff}}}{D_0} \quad (12)$$

holds. A random-walk particle-tracking algorithm [12] is applied in order to simulate D_{eff} for the previously described cubic cut-outs. This method simulates a large number K of independent random walks $r_i(t) = (r_{i,x}(t), r_{i,y}(t), r_{i,z}(t))$ over time in the pore phase, where $r_i(t)$ is the position of the i -th random-walk at time $t > 0$. Then, the normalized effective diffusion coefficient D_{eff}/D_0 is defined by

$$\frac{D_{\text{eff}}}{D_0} = \lim_{t \rightarrow \infty} \frac{1}{2KD_0} \frac{\partial}{\partial t} \sum_{i=1}^K \left(r_{i,z}(t) - r_{i,z}(0) - \frac{1}{K} \sum_{j=1}^K (r_{j,z}(t) - r_{j,z}(0)) \right)^2. \quad (13)$$

Note that $r_{i,z}(t) - r_{i,z}(0)$ is the displacement of the i -th random-walk in z -direction at time t . It is important to note that we consider only displacements in z -direction since mean geodesic tortuosity τ_{geod} and the constrictivity β are computed in z -direction. The accuracy of the random-walk particle tracking algorithm used for the simulation of D_{eff} has been demonstrated in [35–37].

5.3 Results

For each of the two microstructures, we consider 64 (slightly overlapping) cubic cutouts with sizes of $15 \times 15 \times 15 \mu\text{m}^3$. The microstructure characteristics $\varepsilon, \tau_{\text{geod}}, \beta$ and D_{eff} are computed for each of these cutouts, which allows to validate the predictions for $M = \varepsilon D_{\text{eff}}/D_0$ derived by virtual materials testing. While the MAPE is 6% when using Eq. (10), it can be reduced using the predictions obtained by neural networks (2%) and random forests (2%). The neural network and random forest, which are trained in [19], are used for the prediction of $M = \varepsilon D_{\text{eff}}/D_0$. The goodness-of-fit is visualized in Fig. 7. One can observe that $M = \varepsilon D_{\text{eff}}/D_0$ is slightly underestimated by Eq. (10). However, the deviations are not larger than the ones from the virtual microstructures considered in [19].

6 Conclusions

Virtual materials testing is a powerful tool to establish quantitative relationships between microstructure characteristics and functional properties. An overview of results obtained by virtual materials testing to predict effective conductivity by volume fraction ε , mean geodesic tortuosity τ_{geod} and constrictivity β is given. The presented quantitative relationships enable the identification of improved microstructures with respect to effective conductivity. Due to the mathematical analogy, the obtained results can be transferred from conduction processes to Fickian diffusion in order to predict the effective diffusivity in porous microstructures. This is exemplarily demonstrated based on 3D image data of two different microstructures from silica monoliths. The method of virtual materials testing itself is not restricted to conduction processes or Fickian diffusion in two-phase materials. It can also be used to investigate relationships between microstructure characteristics and further functional properties, like e.g. effective permeability or mechanical stress-strain curves.

References

1. DeQuilettes, D., Vorpahl, S.M., Stranks, S.D., Nagaoka, H., Eperon, G.E., Ziffer, M.E., Snaith, H.J., Ginger, D.S.: Impact of microstructure on local carrier lifetime in perovskite solar cells. *Science* **348** (2015) 683 – 686
2. Wilson, J.R., Cronin, J.S., Barnett, S.A., Harris, S.J.: Measurement of three-dimensional microstructure in a LiCoO₂ positive electrode. *Journal of Power Sources* **196**(7) (2011) 3443–3447
3. Prakash, B.S., Kumar, S.S., Aruna, S.T.: Properties and development of Ni/YSZ as an anode material in solid oxide fuel cell: A review. *Renewable and Sustainable Energy Reviews* **36** (2014) 149–179
4. Nischang, I.: Porous polymer monoliths: morphology, porous properties, polymer nanoscale gel structure and their impact on chromatographic performance. *Journal of Chromatography A* **1287** (2013) 39–58
5. Torquato, S.: *Random Heterogeneous Materials: Microstructure and Macroscopic Properties*. Springer, New York (2013)
6. Hashin, Z.: The elastic moduli of heterogeneous materials. *Journal of Applied Mechanics* **29**(1) (1962) 143–150
7. Maire, E., Withers, P.J.: Quantitative X-ray tomography. *International Materials Reviews* **59**(1) (2014) 1–43
8. Holzer, L., Cantoni, M.: Review of FIB-tomography. In Utke, I., Moshkalev, S., Russell, P., eds.: *Nanofabrication using Focused Ion and Electron Beams: Principles and Applications*, Oxford University Press: New York (2012) 410–435
9. Midgley, P.A., Dunin-Borkowski, R.E.: Electron tomography and holography in materials science. *Nature Materials* **8**(4) (2009) 271
10. Chiu, S.N., Stoyan, D., Kendall, W.S., Mecke, J.: *Stochastic Geometry and its Applications*. 3rd edn. J. Wiley & Sons, Chichester (2013)
11. Matheron, G.: *Random Sets and Integral Geometry*. J. Wiley & Sons, New York (1975)

12. Hlushkou, D., Hormann, K., Höltzel, A., Khirevich, S., Seidel-Morgenstern, A., Tallarek, U.: Comparison of first and second generation analytical silica monoliths by pore-scale simulations of eddy dispersion in the bulk region. *Journal of Chromatography A* **1303** (2013) 28–38
13. Doyle, M., Fuller, T.F., Newman, J.: Modeling of galvanostatic charge and discharge of the lithium/polymer/insertion cell. *Journal of the Electrochemical Society* **140**(6) (1993) 1526–1533
14. Holzer, L., Iwanschitz, B., Hocker, T., Keller, L., Pecho, O.M., Sartoris, G., Gasser, P., Münch, B.: Redox cycling of Ni-YSZ anodes for solid oxide fuel cells: Influence of tortuosity, constriction and percolation factors on the effective transport properties. *Journal of Power Sources* **242** (2013) 179–194
15. Shikazono, N., Kanno, D., Matsuzaki, K., Teshima, H., Sumino, S., Kasagi, N.: Numerical assessment of SOFC anode polarization based on three-dimensional model microstructure reconstructed from FIB-SEM images. *Journal of the Electrochemical Society* **157**(5) (2010) B665–B672
16. Tippmann, S., Walper, D., Balboa, L., Spier, B., Bessler, W.G.: Low-temperature charging of lithium-ion cells part I: Electrochemical modeling and experimental investigation of degradation behavior. *Journal of Power Sources* **252** (2014) 305–316
17. Gaiselmann, G., Neumann, M., Pecho, O.M., Hocker, T., Schmidt, V., Holzer, L.: Quantitative relationships between microstructure and effective transport properties based on virtual materials testing. *AIChE Journal* **60**(6) (2014) 1983–1999
18. Stenzel, O., Pecho, O.M., Holzer, L., Neumann, M., Schmidt, V.: Predicting effective conductivities based on geometric microstructure characteristics. *AIChE Journal* **62** (2016) 1834–1843
19. Stenzel, O., Neumann, M., Pecho, O.M., Holzer, L., Schmidt, V.: Big data for microstructure-property relationships: A case study of predicting effective conductivities. *AIChE Journal* **63**(9) (2017) 4224–4232
20. Stoeckel, D., Kübel, C., Hormann, K., Höltzel, A., Smarsly, B.M., Tallarek, U.: Morphological analysis of disordered macroporous–mesoporous solids based on physical reconstruction by nanoscale tomography. *Langmuir* **30** (2014) 9022–9027
21. NM-SESES: <http://nmtec.ch/nm-seses/> (Last accessed date 2017)
22. GeoDict. www.geodict.com (2017)
23. Clennell, M.B.: *Tortuosity: a guide through the maze*. Geological Society, London, Special Publications **122** (1997) 299–344
24. Soille, P.: *Morphological Image Analysis: Principles and Applications*. Springer, New York (2003)
25. VSG - Visualization Sciences Group - Avizo Standard: <http://www.vsg3d.com/> (2017)
26. Petersen, E.E.: Diffusion in a pore of varying cross section. *AIChE Journal* **4**(3) (1958) 343–345
27. Holzer, L., Wiedenmann, D., Münch, B., Keller, L., Prestat, M., Gasser, P., Robertson, I., Grobéty, B.: The influence of constrictivity on the effective transport properties of porous layers in electrolysis and fuel cells. *Journal of Materials Science* **48** (2013) 2934–2952
28. Münch, B., Holzer, L.: Contradicting geometrical concepts in pore size analysis attained with electron microscopy and mercury intrusion. *Journal of the American Ceramic Society* **91** (2008) 4059–4067
29. Møller, J., Waagepetersen, R.P.: *Statistical Inference and Simulation for Spatial Point Processes*. Chapman & Hall/CRC, Boca Raton (2004)

30. Jaromczyk, J.W., Toussaint, G.T.: Relative neighborhood graphs and their relatives. *Proceedings of the IEEE* **80** (1992) 1502–1517
31. Ross, S.: *Simulation*. 5th edn. Academic Press, New York (2013)
32. Stenzel, O., Hassfeld, H., Thiedmann, R., Koster, L.J.A., Oosterhout, S.D., van Bavel, S.S., Wienk, M.M., Loos, J., Janssen, R.A.J., Schmidt, V.: Spatial modeling of the 3D morphology of hybrid polymer-ZnO solar cells, based on electron tomography data. *The Annals of Applied Statistics* **5** (2011) 1920–1947
33. Hastie, T., Tibshirani, R., Friedman, J.: *The Elements of Statistical Learning*. 2nd edn. Springer, New York (2008)
34. Enke, D., Gläser, R., Tallarek, U.: Sol-gel and porous glass-based silica monoliths with hierarchical pore structure for solid-liquid catalysis. *Chemie Ingenieur Technik* **88**(11) (2016) 1561–1585
35. Liasneuski, H., Hlushkou, D., Khirevich, S., Höltzel, A., Tallarek, U., Torquato, S.: Impact of microstructure on the effective diffusivity in random packings of hard spheres. *Journal of Applied Physics* **116**(3) (2014) 034904
36. Hlushkou, D., Liasneuski, H., Tallarek, U., Torquato, S.: Effective diffusion coefficients in random packings of polydisperse hard spheres from two-point and three-point correlation functions. *Journal of Applied Physics* **118**(12) (2015) 124901
37. Daneyko, A., Hlushkou, D., Baranau, V., Khirevich, S., Seidel-Morgenstern, A., Tallarek, U.: Computational investigation of longitudinal diffusion, eddy dispersion, and trans-particle mass transfer in bulk, random packings of core-shell particles with varied shell thickness and shell diffusion coefficient. *Journal of Chromatography A* **1407** (2015) 139–156